THE ASTROPHYSICAL JOURNAL SUPPLEMENT SERIES, 127:333–337, 2000 April

INTERFEROMETRIC AND CHIRPED OPTICAL PROBE TECHNIQUES FOR HIGH-PRESSURE EQUATION-OF-STATE MEASUREMENTS[1]

D. M. GOLD,[2] P. M. CELLIERS, G. W. COLLINS, K. S. BUDIL, R. CAUBLE, L. B. DA SILVA, M. E. FOORD, R. E. STEWART, R. J. WALLACE, AND D. YOUNG
Lawrence Livermore National Laboratory, L-399, Livermore, CA 94550
Received 1999 January 19; accepted 1999 August 5

ABSTRACT

We present experimental work exploring displacement and velocity interferometry as high spatial and temporal resolution diagnostics for measuring target preheat and the speed, planarity, and steadiness of a shock wave. A chirped pulse reflectometry experiment is also proposed as a frequency domain alternative for shock speed measurements. These techniques fill a need for high-precision diagnostics to derive accurate laboratory-based equation-of-state data at shock wave–driven pressures directly relevant to astrophysical systems. The performance of these optical laser probe techniques may exceed conventional passive techniques such as temporally streaked recording of optical emission upon shock breakout or side-on streaked X-ray radiography. Results from Nova laser and high-intensity ultrashort pulse experiments are presented.

Subject headings: equation of state — methods: laboratory — plasmas — shock waves — techniques: interferometric

1. INTRODUCTION

High-precision, $\sim 1\%$, laboratory-scale measurements are critical for accurate discrimination between various predictive equation-of-state (EOS) models that describe materials at pressures found in planetary interiors and brown dwarf stars. With appropriate scaling, these models can connect laboratory EOS measurements using intense lasers to astrophysical problems (Ripin et al. 1990). For example, the EOS of the hydrogen isotope deuterium was recently measured in the laboratory at pressures beyond 2 Mbar driven by a high-power laser (Da Silva et al. 1997). Results demonstrated a significantly higher compressibility near 1 Mbar than predicted by most models as well as evidence of metallic hydrogen behavior (Collins et al. 1998), which supported the earlier discovery of metallization driven by a gas gun (Nellis et al. 1996a, 1996b). This new hydrogen EOS information has a direct bearing on astrophysical models of the composition and formation of Jovian planets and brown dwarf stars.

Achieving precision $\sim 1\%$ presents considerable experimental challenges. High-pressure EOS data are conventionally derived by driving a transient shock wave into a sample and measuring propagation speeds using passive collection of optical emission from shock breakout at the back side of stepped targets, or by radiographically detecting the propagation of contrast differences between shocked and unshocked material. Passive techniques are often limited by their achievable precision, sensitivity, and signal-to-noise ratio. The optical laser probe techniques currently under investigation and described here are designed to exceed the performance of the passive techniques.

Pressures in the astrophysical realm beyond about 1 Mbar can only be achieved by driving transient high-pressure shocks with nuclear explosives or, more practically, high-intensity lasers. Reliable data from lasers depend strongly on the ability to drive a sample along its principle Hugoniot and accurately measure its propagation or breakout time. The principle Hugoniot is the locus of all final states of pressure, energy, and density that are achieved by a single near-ideal shock. Analysis of results obtained from clean principle Hugoniot experiments is particularly simple and accurate (Zeldovich & Raizer 1966). With the initial state specified, conservation relations across the shock require that only two independent parameters be measured to obtain an absolute EOS datum. The shock speed, U_S, particle speed U_p, pressure P, internal energy E, and final density ρ are related by

$$P - P_0 = \rho_0 U_S U_p , \tag{1}$$

$$\rho/\rho_0 = U_s/(U_s - U_p) , \tag{2}$$

$$E - E_0 = \frac{1}{2}(P + P_0)\left(\frac{1}{\rho} - \frac{1}{\rho_0}\right) , \tag{3}$$

where ρ_0 is the initial density, P_0 is the initial pressure, ρ/ρ_0 is the compression, and E_0 is the initial internal energy. Equations (1)–(3) are the Rankine-Hugoniot relations. A near-ideal shock must be steady and planar with extremely low preheat because the Rankine-Hugoniot analysis is only strictly valid under these conditions. Optical probes measure U_s by recording the transit time between shock breakout events on a stepped target with known step heights. U_p is derived by comparing the simultaneously measured shock velocity in two samples with different impedances, a "standard" with a well-known EOS, for example, Al, and a "sample" without. The impedance is ρc_s where c_s is the material's sound speed. The impedance matching method is well described elsewhere (Zeldovich & Raizer 1966). The method is clearly subject to systematic error if the EOS of the standard is not accurately known.

This paper briefly outlines three optical laser probe techniques to measure shock preheat, steadiness, or hydrodynamic expansion upon breakout while simultaneously recording the shock speed and planarity. Section 2 discusses displacement interferometry, which applies a con-

[1] This work was performed by Lawrence Livermore National Laboratory under the auspices of the US Department of Energy under contract W 7405-ENG-48.
[2] gold1@llnl.gov.

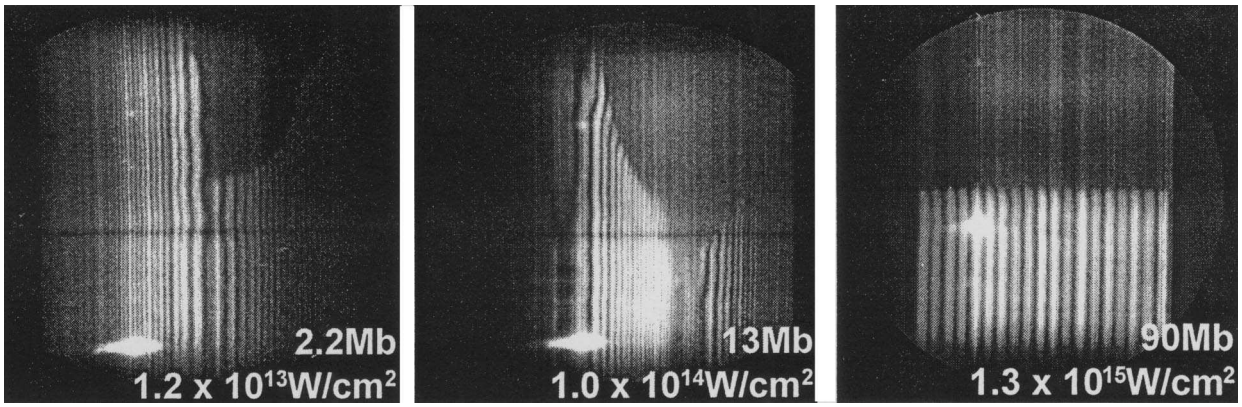

FIG. 1.—Streaked displacement fringes in Si stepped targets directly driven by the Nova laser at three intensities 1.2×10^{13} W cm^{-2}, 1.0×10^{14} W cm^{-2}, and 1.3×10^{15} W cm^{-2} with calculated pressures indicated. The targets were identical with 50 and 100 μm Si steps and a 25 μm CH preheat suppresser with 1000 Å Al vapor deposited on the drive side to prevent Nova laser shine through. Each image is a 10 ns sweep over the central 1 mm of the target breakout region. Laser turn-on occurs $\sim$ 300 ps after the fiducial marker (*bright spot*), and time is swept from bottom to top. At 1.3×10^{15} W cm^{-2} preheat is so large that it vaporizes the entire target before shock breakout.

ventional Michelson interferometer configuration with the shocked sample in one arm to detect preheat, planarity, and shock speed. Section 3 describes velocity interferometry, which measures the steadiness, planarity, and speed of a shock propagating through a transparent material. In § 4 we describe chirped pulse reflectometry, which uses a high-bandwidth optical pulse stretched in time to detect shock speed and expansion dynamics in the frequency domain.

2. DISPLACEMENT INTERFEROMETRY

High-intensity lasers can achieve pressures exceeding hundreds of megabars in macroscopic ($\sim$1 mm) samples. Confidence in these EOS data at pressures beyond a few megabars, however, is usually limited by the ability to minimize preheating of the sample. Preheat from hard X-rays and hot electrons, produced in the intense laser-target interaction, displaces the principle Hugoniot by preparing a higher temperature and lower density state before the arrival of the shock wave. The ability to quantify low levels of preheat is critical to the design of low-preheat driver/target configurations for principal Hugoniot EOS experiments. Sensitive discrimination between various theoretical EOS models demands EOS Hugoniot experiments with a precision $\sim$1% in measured preheat, shock velocities, and target characterization. The uncertainty in the shocked sample's inferred pressure is controlled exclusively by uncertainties in the measured shock velocities or in the sample's initial density and temperature (preheat).

We use a Michelson interferometer to measure the expansion of a laser-driven sample due to preheat. The sample is used as the retroreflector in one arm of the interferometer. The second arm has a flat reference mirror. Each arm contains an identical $f/4$, 20$\times$ relay imaging system arranged so images of the target region and reference mirror overlap at, and fill, the slit of a streak camera. We produce a pattern of straight fringes perpendicular to the slit by tilting the reference mirror slightly from perfect overlap. The image also gives a one-dimensional spatial measurement (along the slit dimension) of shock planarity upon breakout. Preheat causes thermal target expansion, changing the path difference between the sample and the reference arm, shifting the fringe pattern. The interferometric probe is sensitive to a target expansion of approximately ± 0.1 fringes $= \pm 0.05\lambda = 40$ nm, which corresponds to a material-dependent preheat temperature of less than 500°C $\approx$ 0.04 eV. Figure 1 gives an example of results in Si targets with one step. Preheat is below detectable limits at 1.2×10^{13} W cm^{-2} and easily measurable at 1.0×10^{14} W cm^{-2}. Shock breakout at the two steps can clearly be seen at the lower two intensities from the curved disappearance of the fringes as the sample arm reflectivity is destroyed and the sample expands at hydrodynamic release speeds ($\sim 10^6$ cm s^{-1}) orders of magnitude greater than the thermal expansion (sound) speed. Shock speed can be simultaneously calculated by measuring shock breakout times on the structured targets. At the highest intensity (1.3×10^{15} W cm^{-2}) preheat becomes so large that the target's rear surface vaporizes before significant target expansion and before the shock arrives.

3. VELOCITY INTERFEROMETRY

Velocity interferometry directly measures the propagation speed of a shock through a transparent material by recording the Doppler shift imparted to a probe beam reflected from the ionized shock front (Collins et al. 1998). The Doppler shift is manifested as fringe motion in an interferometric signal when it is mixed with light from the unshifted reference arm. It is important to note that direct optical measurement of a propagating shock demands a high reflectivity. Laser-driven shock research has attained shock amplitudes well above megabar pressures, which easily creates high-reflectivity ionizing shock fronts.

A simple description of a velocity interferometer is derived from considering a standard Michelson interferometer configuration with *unbalanced* arms. One arm contains an extra path length $2L = c\tau$, where L is the arm displacement, c is the speed of light, and τ is the time delay. The optical phase difference ϕ in the arms is

$$\phi = \frac{2\pi}{\lambda}(2L) = \frac{2\pi}{\lambda}(c\tau) . \tag{4}$$

Small changes in this optical phase difference create fringe shifts where the signals are mixed at the detector:

$$|d\phi| = \frac{2\pi c\tau}{\lambda}\left|\frac{d\lambda}{\lambda}\right| . \tag{5}$$

If one of the interferometer arms is now allowed to move, the Doppler shift is of magnitude

$$\left| \frac{d\lambda}{\lambda} \right| = \frac{2u}{c}, \tag{6}$$

so the phase shift is

$$|d\phi| = \frac{4\pi\tau}{\lambda} |u| . \tag{7}$$

The fringe shift in the interference pattern is directly proportional to the velocity of the moving target.

A small modification of this configuration allows Doppler shifts of spatially incoherent light to be measured. This is significantly more practical for measurements involving motion of targets with rough or nonplanar surfaces as encountered with shock breakout experiments. The Velocity Interferometer System for any Reflector (VISAR) configuration (Barker & Hollenbach 1972) places a delay etalon in one interferometer arm such that when viewing into the interferometer the arms *appear* to be equal; however, the recombined beams are temporally delayed relative to each other (unbalanced arms). The effect allows white light (spatially incoherent signals) interferometry *and* velocity (Doppler-shifted signals) interferometry.

Our velocity interferometer system employed a Mach-Zehnder configuration with a delay etalon in one arm. The reference mirror and delay element were mounted on a translation stage, fitted with a precision motorized micrometer screw, to adjust the path in the delay arm. Initially we set the path length of this arm (etalon removed) equal to that of the other arm by looking for white light fringes in the interferometer output (~ 1 μm precision). We then inserted the delay element and moved the mirror back a distance equal to $(1 - \frac{1}{n})h$, where n is the refractive index of the etalon and h is its thickness. The total optical path difference is then equal to $d = (n - \frac{1}{n})h$, and the precision in this setting is ± 3 μm, limited by the reproducibility of the motorized screw.

The fringe phase, ϕ (in radians), produced by the velocity interferometer is related to the velocity, u, of the reflecting surface through the velocity interferometer equation $u = \lambda\phi/4\pi\tau$, where λ is the laser wavelength, and τ is the delay in the velocity interferometer. The precision of this measurement is determined by the accuracy in determining λ, τ, and ϕ. It is important to note that this is independent of the sweep calibration in the streak camera and independent of target design and/or metrology. Accuracies better than 1% are easily achievable; for example, a 20 km s^{-1} shock can be measured with 1% (0.2 km s^{-1}) accuracy using a velocimeter with 7 km s^{-1} fringe^{-1} sensitivity by measuring the phase to an accuracy of 0.2 fringe. In practice, the phase can be extracted with better than 0.1 fringe accuracy from the interferograms we have recorded. We believe that the precision could approach 0.01 fringe with high-quality data and sophisticated phase detection software routines.

An example recording of a streaked interferogram from our VISAR system is shown in Figure 2. The target is a laser-driven Al pusher unloading a shock into liquid deuterium. We observe the shock trajectory in the transparent liquid deuterium. Details of the experiment are found in Da Silva (1997). For negative times on the scale in Figure 2*a*; the recording shows the reflection from the Al pusher surface prior to the emergence of the shock into the deuterium sample. The data is both space- and time-resolved: in this particular case, the drive beam focus was slightly nonuniform and therefore produced a spatial variation in the breakout time at the pusher deuterium interface, which is readily observable in the image. When the shock emerges from the Al interface the reflected signal drops simultaneously with a shift of the fringe pattern to a new phase. For positive times, the recording shows light reflected from the shock front. There is an ambiguity in determining the initial phase shift at the moment of shock breakout, because the streak camera cannot resolve the fringe motion quickly enough during the 75 ps (equal to the interferometer delay) that it takes for the fringes to move the new phase. When the etalon delay is set for high sensitivity, the initial phase shift can be several fringes. In this particular experiment we can resolve this ambiguity by comparing the velocimetry data with a side-on radiograph of the shock trajectory as described in Da Silva (1997): at shock breakout the initial phase shift is 2.7 $\pm$ 0.05 fringes, giving shock speed of 18 km s^{-1}. In the absence of an independent diagnostic, this ambiguity can also be resolved by splitting the reflected light and

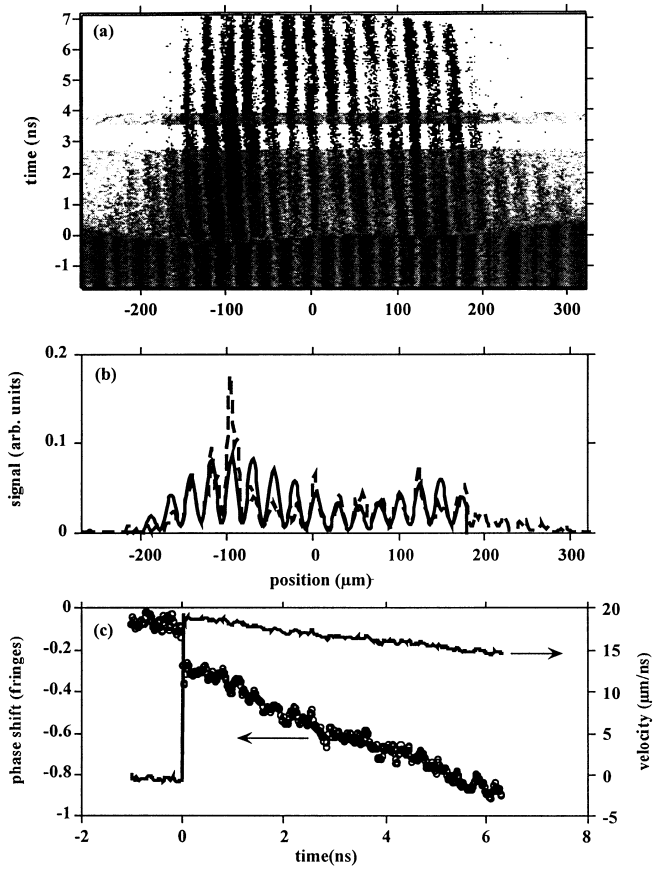

FIG. 2.—(*a*) Example of a streaked VISAR interferogram recorded for a decaying shock front. The initial phase shift is approximately 2.7 fringes to the right, followed by a continuous shift to the left (deceleration) of approximately 1 fringe after 6 ns. (*b*) Interferogram intensity as a function of position measured (*dashed line*) and fitted (*solid line*) at time 2 ns, indicated by the horizontal line in (*a*). The horizontal scale is matched to that scale in the image. (*c*) Extracted phase from the record is (*a*) as a function of time, at the central position 0 (μm). The open circles show the raw phase shift (in radians, modulo 2π), that was extracted from a series of fits similar to that in (*b*) performed across the entire image. The initial phase offset for $t < 0$ was subtracted. The solid line shows the velocity extracted from the raw phase, after applying a correction of $+3$ fringes to the raw phase.

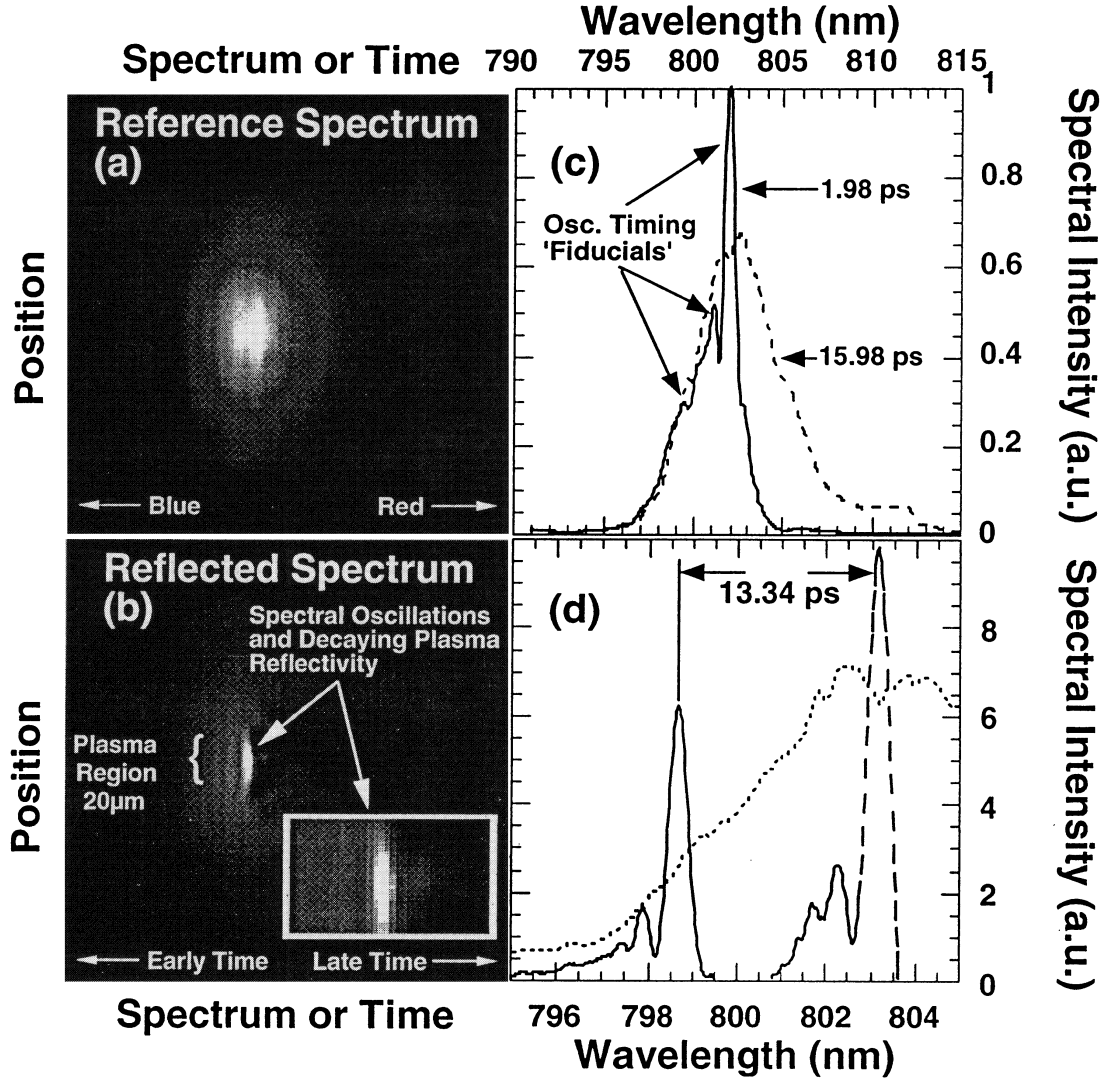

FIG. 3.—Results of a CPR measurement. (*a*) Spatially resolved reference spectrum is negatively chirped to a pulse width of 15.98 ps FWHM at a chirp rate of 0.32 nm ps^{-1}. (*b*) Spatially resolved reflected spectrum shows the plasma interaction region in the central 20 μm of the illuminated field (*magnified in the inset figure*). (*c*) Lineouts across the central plasma region for the reference (*dotted line*) and reflected (*solid line*) spectra (upper wavelength axis). The reflected spectrum has spectral oscillations, which can be used as shock breakout timing fiducials, and a reflection decay, which is discussed in the text. (*d*) Magnified spectral oscillations at two times separated by 13.34 ps (*dashed and solid lines*), and the reference spectrum (*dotted line*) (lower wavelength axis). Calibration gives a time resolution of 88 fs $pixel^{-1}$ or 3.024 ps nm^{-1}. Time differences between the respective three peaks and two valleys in the spectra can be averaged to increase timing precision. The spectral intensity scale in (*d*) is arbitrary because oscillations have been shifted vertically for comparison.

passing it through two velocity interferometers with different sensitivities (etalon delays).

4. CHIRPED PULSE REFLECTOMETRY

A "chirped" pulse is a high-bandwidth pulse that has been stretched in time by forcing different frequencies to travel different path lengths with spatial dispersion optics such as gratings or prisms. Chirped pulse reflectometry (CPR) is a frequency domain technique that times shock breakout by recording the reflectivity change at breakout as a modulation in the spectrum of a chirped optical probe pulse. The breakout time is encoded in the spectrum of a chirped probe pulse reflected at the shocked surface. If the frequencies of the chirped pulse change linearly with time, event timing is directly proportional to the frequency at which the reflectivity changes sharply. Spectral oscillations also appear due to a near discontinuous change in reflectivity in the time domain. Spectral oscillations act as precision relative timing fiducials. These fiducials are reproducible because they depend only upon the probe chirp rate and the shock breakout dynamics. In addition, taking the square root of the modulated spectrum intensity measured by the spectrometer, multiplying by stretcher-induced and plasma reflection–induced phase, and Fourier-transforming gives a complete plasma reflectivity or shock breakout time history during the chirped pulse. The plasma reflection–induced phase is measurable with a high-precision spectral domain interferometry technique recently demonstrated (Blanc et al. 1996). Spatially imaging the probe interaction region onto a spectrometer slit allows simultaneous measurement across all probed target regions. Simultaneously recording breakout times in target regions with steps of different, but accurately known, thicknesses, constitutes a direct shock speed measurement. Note that CPR avoids the sensitivity, dynamic range, signal-to-noise ratio, and nonlinearity problems associated with streak camera–based measurements. CPR has the potential of measuring shock speeds over hundreds of picoseconds with

a time resolution less than 100 fs, giving a precision of $\sim 0.1\%$.

CPR was tested by using the formation of an initially ultrashort scale length, aluminum plasma ionized by a pump pulse to simulate a reflectivity change ($\sim 40\%$ at $[T_e]_{\rm peak} \sim 1$–35 eV) comparable to an ionizing shock breakout. The target consisted of a 5 μm aluminum layer coated onto 0.0625 thick fused quartz substrate. The pump was a frequency-doubled 400 nm, 130 fs pulse focused to $\sim 10^{14}$ W cm^{-2} at normal incidence, while the unchirped probed was picked off from the fundamental, 800 nm, pump beam at nonintrusive microjoule pulse energies. The probe pulse was negatively chirped in a double-pass grating pair stretcher to $\sim$ 15–20 ps, reflected from the plasma, and imaged onto a spectrometer slit with a 30$\times$ magnification factor. The measured spatial resolution was 3 μm. The probe was spatially filtered and apertured to obtain a smooth focal spot many times larger than the plasma region. Both pulses were focused by a silver off-axis parabolic mirror (pump f/7.5, probe greater than f/70). Pulse overlap was monitored by 20$\times$ magnification back-imaging system and video camera. Temporal delay between the pump and probe was adjusted by an optical delay line. The 800 nm probe signal was separated from scattered 400 nm pump light by spectral dispersion in the spectrometer. Spectra were recorded with a 12-bit CCD camera head placed at the focal plane of the spectrometer. Chirp calibration was determined by the wavelength at which spectral features in the reflected spectrum appeared at known time delays on the absolutely calibrated spectrometer.

Raw CPR data in Figure 3 shows the plasma reflection history in one spatial dimension. The reference spectrum (Fig. 3*a*) is negatively chirped to a pulse width of 15.98 ps FWHM at a chirp rate of 0.32 nm ps^{-1}. The reflected spectrum (Fig. 3*b*) clearly shows the plasma interaction region in the central 20 μm of the illuminated field, which is magnified in the inset figure. From lineouts across the central plasma region (Fig. 3*c*), no spectral modulation is observed until the pump pulse arrives and plasma is formed at approximately the temporal center of the chirped pulse. Upon plasma formation, the reflectivity drops rapidly ($\sim$ 100 fs) to approximately 60% of its cold value, producing several distinct spectral oscillations, followed by a small tail of decaying reflection. The tail of reflectivity decay is caused by absorption and scattering during plasma expansion after several picoseconds, when the plasma has a significant scale length (Ng, Forsman, & Celliers 1995). This decay time is in good agreement with simulations performed for aluminum at $\sim 10^{14}$ W cm^{-2} using the LASNEX (Alley 1991) one-dimensional Lagrangian hydrodynamic code. The oscillations at two different time delays separated by 13.34 ps are shown magnified in Figure 3*d* to illustrate the temporal accuracy and precision of the technique. The widths and wavelengths of the spectral oscillations are nearly identical because the oscillations depend only upon the probe pulse chirp and the plasma dynamics, which vary only with laser fluctuations. Oscillation signals are well separated, and three peaks are easily seen at each plasma formation time. This temporal separation on a stepped aluminum target for shock experiments at $\sim$ 10 Mbar (shock velocity $\sim$ 24.5 μm ns^{-1}) would correspond to a target step height of 0.33 μm, easily achievable with current target fabrication technology. The ultimate temporal resolution is determined by the input pulse width, chirp rate, spectrometer spectral dispersion, and the detection camera pixel size. For example, using a high-resolution spectrometer (0.66 m focal length, 1800 grooves mm^{-1} grating) with a reciprocal linear dispersion of $\sim$ 10 Å mm^{-1} and a camera of pixel size of $\sim$ 25 μm at the chirp rate of 0.32 nm ps^{-1} used in this experiment, a time resolution of $\sim$ 78 fs pixel^{-1} is achievable. Thus the achievable temporal precision is less than 1% over a record length of 20 ps.

In a shock velocity or impedance matching experiment, the time separation between these breakout signals would depend on the path length and shock impedance in a stepped target. Instead of seeing signals from two probes at different times, one would have a single probe at a fixed time, and signals coming out at two different times would be separated spatially by imaging onto the spectrometer slit. Finally, it is worth noting that CPR can also determine the dynamics of shock breakout and the subsequent hydrodynamic expansion. Fourier inversion of the spectrum can be used to obtain a single-shot measurement of reflectivity time history over many picoseconds. Although the phase shift due to plasma reflection must be known accurately for inversion, recent measurements using spectral domain interferometry have shown this to be possible for short scale length plasma expansion such as that encountered during the initial breakout.

5. SUMMARY

Using laser-driven shock waves to study materials at pressures relevant to astrophysics depends critically on the ability to accurately and precisely diagnose details of the shock. Impedance-matched principle Hugoniot measurements offer a simple analysis of complex high-pressure systems, but preheat and shock speed, planarity, and steadiness must be well known to be controlled and for the analysis to be applicable. Optical probes address these issues. Displacement interferometry is the most sensitive preheat diagnostic available and thus is critical at higher pressures where copious X-ray and hot electron preheat can be generated. Extremely accurate measurements of shock trajectories through transparent samples, including astrophysically important hydrogen, are possible with the VISAR technique. Chirped pulse reflectometry offers a frequency domain approach to measuring shock speed with some advantages in signal detection because it does not rely on a streak camera. All three techniques have the necessary precision of less than 1% to discriminate between EOS models, which are the most accessible route to insight into some astrophysical problems.

REFERENCES

Alley, W. E. 1991, Proc. SPIE, 1413, 89
Barker, L. M., & Hollenbach, R. E. 1972, J. Appl. Phys., 43, 4669
Blanc, P., et al. 1996, J. Opt. Soc. Am. B, 13, 118
Collins, G. W., et al. 1998, Science, 281, 1178
Da Silva, L. D., et al. 1997, Phys. Rev. Lett., 78, 483
Nellis, W. J., et al. 1996a, Phys. Rev. Lett., 76, 1860
Nellis, W. J., et al. 1996b, Science, 273, 936
Ng, A., Forsman, A., & Celliers, P. M. 1995, Phys. Rev. E, 51, 5208
Ripin, B. H., et al. 1990, Laser Part. Beams, 8, 183
Zel'dovich, Y. B., & Raizer, Y. P. 1966, Physics of Shock Waves and High-Temperature Hydrodynamic Phenomena (New York: Academic)